

Research Article

Performance Analysis of a Relift Luo Converter-Derived Dual-Output DC to DC Converter for Microgrid Applications

R. Banupriya¹ and R. Nagarajan ²

¹Department of Electrical and Electronics Engineering, PGP College of Engineering and Technology, Tamil Nadu, India

²Department of Electrical and Electronics Engineering, Gnanamani College of Technology, Tamil Nadu, India

Correspondence should be addressed to R. Nagarajan; krnaga71@yahoo.com

Received 1 April 2022; Revised 16 September 2022; Accepted 5 October 2022; Published 4 November 2022

Academic Editor: Jegadesan Subbiah

Copyright © 2022 R. Banupriya and R. Nagarajan. This is an open access article distributed under the Creative Commons Attribution License, which permits unrestricted use, distribution, and reproduction in any medium, provided the original work is properly cited.

A microgrid typically maintains multiple voltage bus bars with AC or DC or both. The various subsystems participating in the microgrid are connected to the appropriate voltage bus bars. Renewable energy sources like the wind energy or the solar photovoltaic energy may also be integrated to the microgrid. A battery-based energy storage system is also usually required. In this work, a dual-output DC to DC converter derived from the double lift or the relift Luo converter is proposed and validated. The proposed system uses a solar photovoltaic source and delivers a high-voltage DC output to deliver power to the high-voltage DC bus bar. A battery of medium voltage is connected across the second output of the dual-output converter. The proposed idea is validated using modeling and simulations in the MATLAB Simulink environment and an experimental prototype.

1. Introduction

Microgrids are drawing attention from engineers and scientists during the last few decades. A microgrid integrates a number of loads and sources used in a specific system like an automobile, an aeroplane, a satellite launch vehicle, and a satellite. There could be DC and AC bus bars running around where the sources and loads with appropriate voltage ratings connected. Microgrids usually include renewable energy sources. The renewable energy sources deliver power into the microgrid using power electronic converters so that the harvested energy is appropriately voltage transformed and pumped into the bus bars with different voltage ratings. Battery-based storage elements are also required in a microgrid so that the renewable energy harvested from the solar photovoltaic source can be stored during the periods while the solar irradiance is available, and the stored energy can be used during the periods while the solar energy is not available, particularly during the night.

Since the microgrid includes voltage bus bars of AC and DC voltages with high- and low-voltage channels, it is necessary that multiple output power electronic converters be employed. For example, if a microgrid may have two isolated DC bus bars with 12 V and 40 V ratings, then the renewable energy harvested may be routed to both these bus bars with the intention of sharing the harvested energy among the bus bars using a dual-output DC to DC converter. Similarly, a microgrid may use two AC bus bars with 48 V and 110 V AC 50 Hz bus bars, then the available renewable energy which could be in the DC form could be shared using an inverter with multiple outlets. So many topological variants for multiple output power conversion systems and control schemes for a variety of applications have been reported in the literature, and some of the milestone contributions are reviewed herein so that the research gaps could be identified. In the year 2013, Chen et al. [1] developed a three-port DC-DC converter with high voltage gain. The authors have demonstrated how it could be used for

battery-charging powered from a solar photovoltaic source. A novel DC to DC converter topology with a high power conversion efficiency and wide range of operation with zero voltage switching and lower output inductance has been proposed and validated by Lin and Chu [2]. Dung et al. [3] focused on the development of a strategic control scheme for a DC to DC converter that can transact power in either direction. Further, Choudhury et al. [4] developed a hybrid energy-supported DC to DC converter topology with three ports featuring soft switching and nonisolation among the ports.

For the purpose of achieving increased voltage gain and isolation between the input and the output sides of DC to DC converters, a resonant AC link between the input and the output stages is often promoted by many researchers. Series LCL or LLC types of resonant converters have also been advanced by many researchers. Resonant AC link-based DC to DC converter schemes offer the advantages of increased voltage gain and a two-pronged control system implemented in the input and the output stages of conversion as well as galvanic isolation between the source and the load. Resonant converters and partial resonant converters offer ZVS or ZCS feature which increases the overall power conversion efficiency by reducing the switching losses. Malan et al. [5] have demonstrated a quasiresonant DC to DC converter and have exhibited the reduction of switching losses. A novel multiport zero voltage switched DC to DC converter featuring zero voltage switching has been proposed and validated by Faraji and Farzanehfard [6].

With the intention of maximum usage of the source and the reduction of ripple on the output voltage, the interleaved DC to DC converter systems have also been developed by many authors. In the research article [7], a novel interleaved DC to DC converter with the features of expandability and high voltage gain and reduced switching losses has been demonstrated. Besides, transformers and coupled inductors play an important role in the design and development of high voltage gain multiport DC to DC converters. Babaei et al. [8] have developed a DC to DC converter with a three winding coupled inductor that provides nonisolation, reduced voltage stress, and high voltage gain features. Increased voltage gain and reduced switching losses, minimal ripple on the output DC voltage, and linearity in control for maximum possible range of output voltage and loading conditions are some of the basic requirements of a power electronic converter. In this consideration, several authors have derived novel conversion schemes using the traditional converters like the SEPIC converter, the Ćuk converter, and the Luo converter. For example in reference [9], Saadatizadeh et al. have modified the basic SEPIC topology for getting high voltage gain. Further, the authors have developed high voltage gain quasi-SEPIC converter.

Interestingly, the DC to DC converters of different design aspects have been used by researchers for integrating the solar photovoltaic energy or any other DC source with the microgrid or the national grid through the DC link of the DSTATCOM or the DVR. In such cases, a bidirectional buck boost converter suitable for including a battery-based storage scheme has also been used and such an implementa-

tion has been carried out by the Mahmoudi et al. [10]. Park et al. [11] have developed a three-port DC to DC converter for a standalone solar photovoltaic system. Yet, another multiport DC to DC converter scheme supported by solar photovoltaic source is reported in [12]. Integration of solar photovoltaic energy into the grid through a synchronously operating inverter with a front end generic boost DC to DC converter has been presented by the authors in [13].

A multifunction converter powered from a solar photovoltaic source primarily for water pumping applications has been developed by Ravichandrudu et al. [14]. An artificial neural network-controlled battery charging system has been proposed and validated by Vasquez et al. [15]. A hybrid energy storage system powered from the solar photovoltaic system has been developed by the authors in [16]. Similarly, in [17], a solar-powered battery-based energy storage system has been designed for applications in AC low-voltage systems and for catering power for nonlinear load applications. Taneja [18] made a detailed study on the power electronic conversion systems powered by a solar photovoltaic source. The author of this work made the study in the perspective of reliability study. The work by Singh [19] enabled the design of a solar photovoltaic simulator so that the research activities related to solar photovoltaic energy conversion systems could be carried out seamlessly in a laboratory during day or night.

Multiport DC to DC converters have been extensively suggested for use in microgrids as well. In the research article [20], Mahadik developed a harmonic reduction scheme for a cascaded cell-based islanded microgrid. In [21], the authors have developed a high step up DC to DC converter with a Ćuk-derived quadratic boost converter. Various configurations of multiple output DC to DC converter have been discussed in article [22]. A quadratic boost converter with high voltage gain has been presented by Lee et al. [23]. From the available literature, it can be made out that the multiport DC to DC converters have been used for a variety of applications. There are different topologies and control systems adopted for multiport DC to DC converters. Multiport DC to DC conversion systems have been developed based on the generic boost converter or the quadratic boost converter (QBC) or the SEPIC converter. But in most applications, one of the ports is used for charging a storage battery and usually this port is of bidirectional nature, so that in the absence of the renewable energy sources or the absence of utility source from the grid, the battery can be used for powering up the load.

In this work, the double lift or the relift Luo converter is considered for a possible development of a multiport DC to DC converter with the intention of developing high- and low-voltage channels for applications in an electric vehicle. The proposed system can harvest the solar photovoltaic energy and store it in a battery, and in the absence of the solar PV source, the battery can be used for accessories operated from a low voltage as well; the traction motor can be driven by the high-voltage channel. This article presents the state space modeling, the circuit modeling of the proposed system, and the proposed idea has been validated using an experimental prototype.

The paper has been arranged as follows. Next to this introduction given as Section 1, Section 2 gives an outline of the proposed system. Section 3 presents the details of the proposed system. Section 4 presents the details of implementation of the proposed system in MATLAB Simulink. Section 5 gives the details of the prototype developed to validate the proposed system and the results obtained thereof. The conclusion and the references follow.

2. Proposed System

Figure 1 shows the block diagram of the proposed system. It is a relift Luo converter-derived buck boost converter. The core of the proposed system is the relift Luo converter. An additional synchronous buck boost converter is inserted between the two stages of the relift converter. The bidirectional converter is used to charge a battery when the main source of power is available and to supply power from the battery to the load when the main source is not available. The main source of power is a solar photovoltaic source. The system can be operated in many modes. The battery can be charged from the solar photovoltaic source while the first stage of the relift converter is just an uncontrolled passage, and the synchronous buck boost converter controls the charging of the battery. When the solar PV source is not available, the battery powers up the load through the buck boost converter and the second stage of the relift converter.

The proposed system has been demonstrated with a resistive load connected across the regulated output voltage of 48 V. The solar photovoltaic source is used to drive the load as well as charge the battery. When the solar source is not available the battery may drive the load. The maximum load considered is 120 Watts, and the maximum capacity of the solar source is around 390 Watts. The solar source can deliver power to the load as well as charge the battery. As for the control system, the sliding mode control scheme is used for both maximum power point tracking of the solar photovoltaic source as well as regulating the output voltage across the load. The details of the operation of the proposed system under different scenarios are discussed in the following sections.

2.1. Topology of the Proposed System. Figure 2 shows the topology of the proposed system. The relift converter is the core of the system. It comprises of a set of two parallel charge and series discharge circuits. The first set comprises of the inductor L1 and capacitor C1. Capacitor C2 is an intermediate DC link capacitor between the two stages. The second stage or the relift stage comprises of the inductor L2 and capacitor C3 in the parallel charge and series discharge circuit with the capacitor C4 as the final filter capacitor.

The switch Q1 is the usual power control switch of the relift Luo converter. Switches Q2 and Q3 are used in the synchronous buck boost converter. The battery charging circuit draws power from the intermediate point in between the two stages of the relift Luo converter. The intermediate voltage across capacitor C2 assumes two different values depending upon whether the power control switch Q1 of the relift Luo

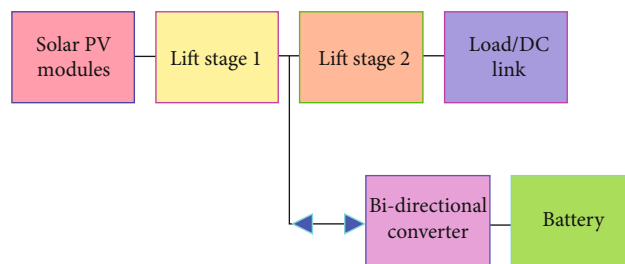


FIGURE 1: Block diagram of the proposed system.

converter is working or not. While the load requires power, the relift Luo converter is operational and the voltage across the C2 is higher than it would be when there is no load and Q1 is not operational. The battery charging current is controlled by the buck converter switch Q2, which is working in synchronism with the other switch Q3. When the solar PV source is not available, the switches Q2 and Q3 operate and power is delivered to the intermediate point across C2. Further, the voltage across C2 is relifted by the action of the switch Q1 so as to deliver the required voltage across the load.

The complete topology of the proposed system can be considered three sections. The first lift section terminated across C2, the synchronous buck boost section, and the second lift section from C2 to the final load and the filter capacitor C4. The voltage gain of the front end lift converter is given as

$$\frac{V_{\text{out}}}{V_{\text{in}}} = \frac{2-k}{1-k}. \quad (1)$$

In Equation (1), k is the duty cycle applied at Q1. Similarly, the voltage gain of the second stage is also given as Equation (1). The overall voltage gain of the relift Luo converter is given as

$$\frac{V_{\text{out}}}{V_{\text{in}}} = \left(\frac{2-k}{1-k} \right)^2. \quad (2)$$

For a duty cycle of 0.5, the theoretical overall voltage gain of the relift converter is 9. However, because of the voltage drops occurring in the diodes and the other passive components, the voltage gain is reduced and is as shown and discussed later in Figure 3 where the duty cycle versus V_{out} plot of the relift Luo converter is presented. It has been observed that an output voltage of 72 V was obtained for a duty cycle of 0.5 while the input voltage is 12 V. This accounts to a practical voltage gain of 6 against the theoretical voltage gain of 9 for a duty cycle of 0.5. The voltage gain of the buck converter is given by Equation (3), and the voltage gain of the generic boost converter is given by Equation (4) in the following:

$$\frac{V_{\text{out}}}{V_{\text{in}}} = d, \quad (3)$$

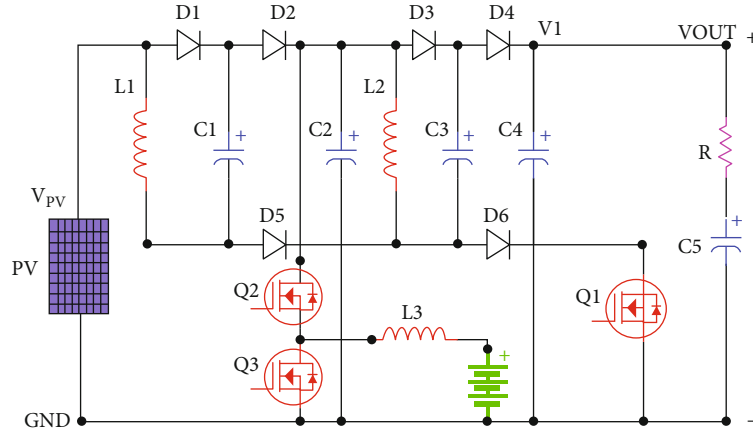


FIGURE 2: Topology for including a battery backup investigated with a relift Luo converter.

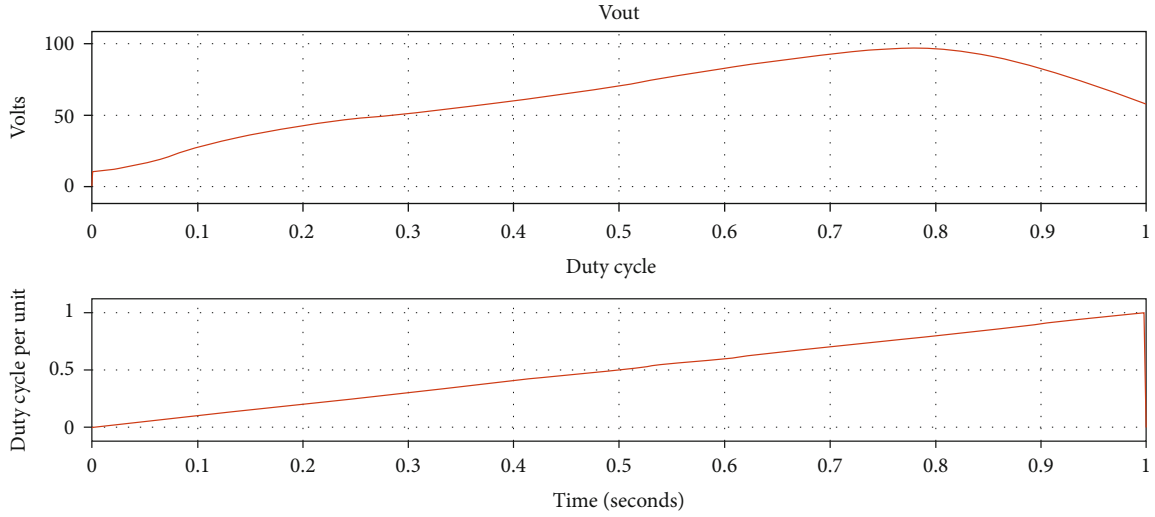


FIGURE 3: Plot of the output voltage vs. duty cycle changed from 0 to 1.

$$\frac{V_{\text{out}}}{V_{\text{in}}} = \frac{d}{1-d}. \quad (4)$$

2.2. State Space Analysis of the Proposed Topology. The state space analysis of the proposed system has been carried out in a sectionalized manner. In the first section, the front end lift converter is considered. V_{in} is the main input voltage, and the output of the first stage is terminated across the capacitor C2. The voltage across the capacitor C2 is the input for the second stage as well as the buck boost converter formed using the switches Q2 and Q3. The state analysis has been done for the individual lift stages.

The switch Q1 is common for both the the front and the rear end lift sections. For the front end lift converter, an equivalent load of $R = 10$ Ohms has been considered. Considering Figure 4(a), the front end lift converter has an input voltage of V_{in} , a load resistor R , the switch Q1, the diodes D1 and D2, and the passive components L1, C1, and C2. For this section, there are three state variables and the strate equation can be derived using the fundamental Kirchoff

equations applied to the two modes of the circuit as shown in Figures 4(b) and 4(c).

The averaged state space model for the first lift stage is shown in

$$\begin{bmatrix} \frac{diL1}{dt} \\ \frac{dvC1}{dt} \\ \frac{dvC2}{dt} \end{bmatrix} = \begin{bmatrix} \frac{1}{RinL1} & \frac{d-1}{L1} & \frac{d-1}{L1} \\ \frac{1-2d}{C1} & \frac{-d}{RinC1} & 0 \\ \frac{1-d}{C2} & 0 & \frac{-1}{RC2} \end{bmatrix} * \begin{bmatrix} iL1 \\ vC1 \\ vC2 \end{bmatrix} + \begin{bmatrix} \frac{1}{L1} \\ \frac{d}{RinC1} \\ \frac{iL1}{C2} \end{bmatrix} * [V_{\text{in}}]. \quad (5)$$

In Equation (5), d is the duty cycle and Rin is the source resistance which is extremely small. The value of $L1 = 12$ mH, $C1 = C2 = 2200$ microfarad, and $R = 48$ Ohms. In a similar manner, the second lift section starts from capacitor C2 and ends at the high voltage load of 24 or 48 Ohms.

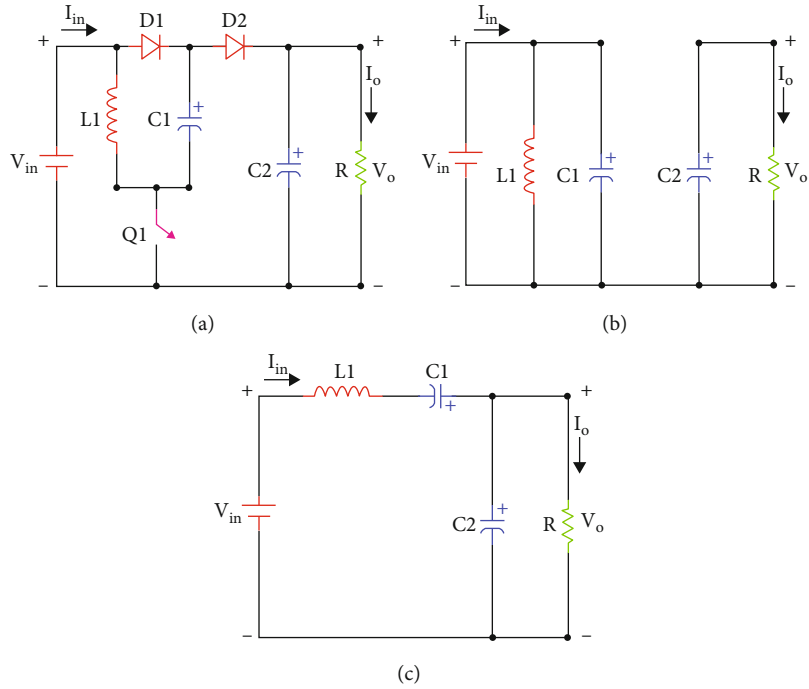


FIGURE 4: (a) First lift stage 3. (b) Switching mode-1 3. (c) Switching mode-2.

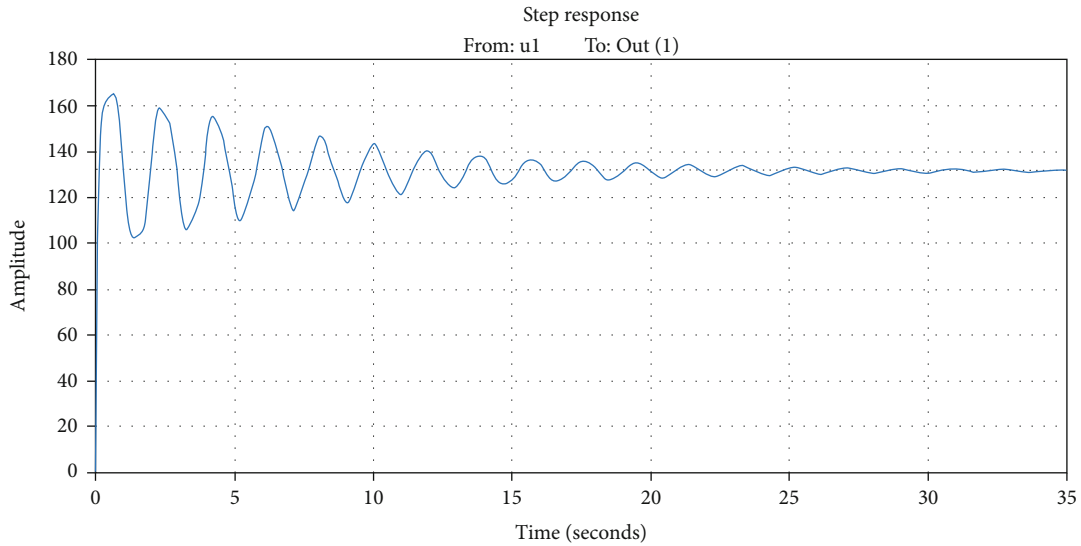


FIGURE 5: The step response of the transfer function sys.

The averaged state space model for the load side lift stage is shown in

$$\begin{bmatrix} \frac{diL2}{dt} \\ \frac{dvC3}{dt} \\ \frac{dvC4}{dt} \end{bmatrix} = \begin{bmatrix} \frac{1}{RinL2} & \frac{d-1}{L2} & \frac{d-1}{L2} \\ \frac{1-2d}{C3} & -d & 0 \\ \frac{1-d}{C4} & 0 & \frac{-1}{RC4} \end{bmatrix} * \begin{bmatrix} iL2 \\ vC3 \\ vC4 \end{bmatrix} + \begin{bmatrix} \frac{1}{L2} \\ \frac{d}{RinC3} \\ \frac{iL2}{C4} \end{bmatrix} * [V_{in}]. \tag{6}$$

In Equation (6), d is the duty cycle and Rin is the source resistance which is extremely small. The value of $L2 = 12$ mH, $C3 = C4 = 2200$ microfarad, and $R = 48$ Ohms. In Equation (6), the input voltage V_{in} is actually the voltage drop across the capacitor $C2$ of the first stage. The voltage across capacitor $C2$ is actually the DC bus bar voltage where the battery section buck boost converter is connected. The output of the first stage of the lift converter can be used for other standalone loads.

The third section is the buck boost converter comprising of the switches $Q2$ and $Q3$ along with the battery and the

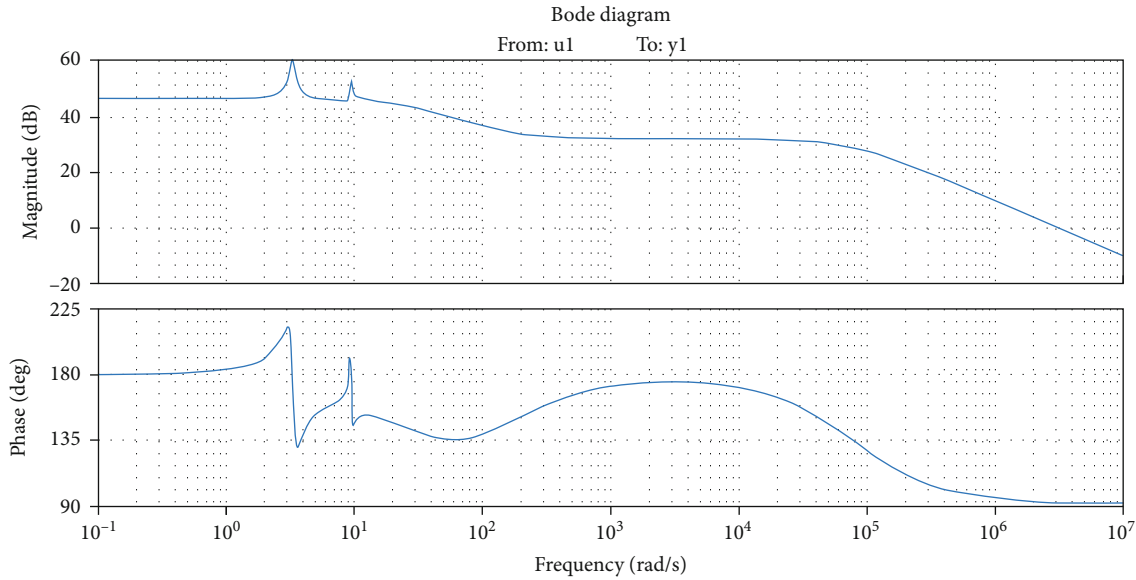


FIGURE 6: The Bode plot of the transfer function sys.

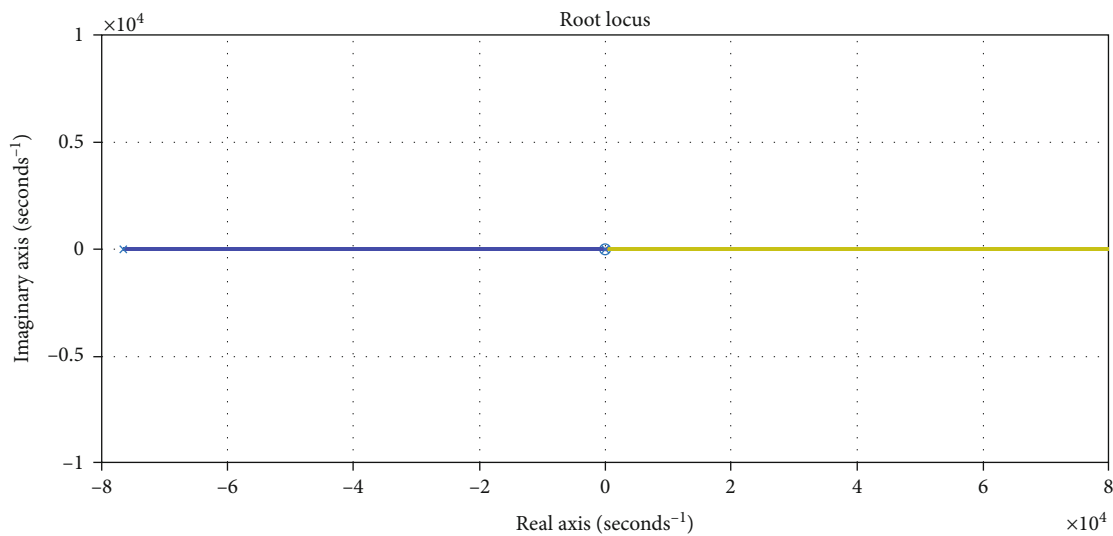


FIGURE 7: Root Locus of the transfer function sys,

inductor L3. The battery can be charged from the voltage across C2 when the main source of voltage V_{in} is available. If V_{in} is not available, then the battery energizes the capacitor C2, and it is further stepped up by the second lift stage, and the final 48 V load is thus fed from the battery. During the boost mode, switch Q3 is operational and Q2 is turned off. The internal diode of Q2 is used as the reversed blocking diode. Since there are two switches, Q2 and Q3, in the battery control buck boost converter stage, there are four possible combinations of these switches.

(i) *Combination 1.* Q2 = Q3 = off. This mode is treated as a standby mode. Only the two stages of the relift converter are now operational

(ii) *Combination 2.* Q2 = active and Q3 = off. In this mode, only buck operation is done. Energy flows from the first stage of the relift converter to the battery so as to charge the battery. The state analysis of this mode is much similar to that of the generic buck converter. The internal diode of Q3 is acting as the freewheeling diode

(iii) *Combination 3.* Q2 = off and Q3 = active. In this mode, only boost operation is done. Energy flows from the battery to the load through the second stage of the lift converter. The state analysis of this mode is much similar to that of the generic boost converter

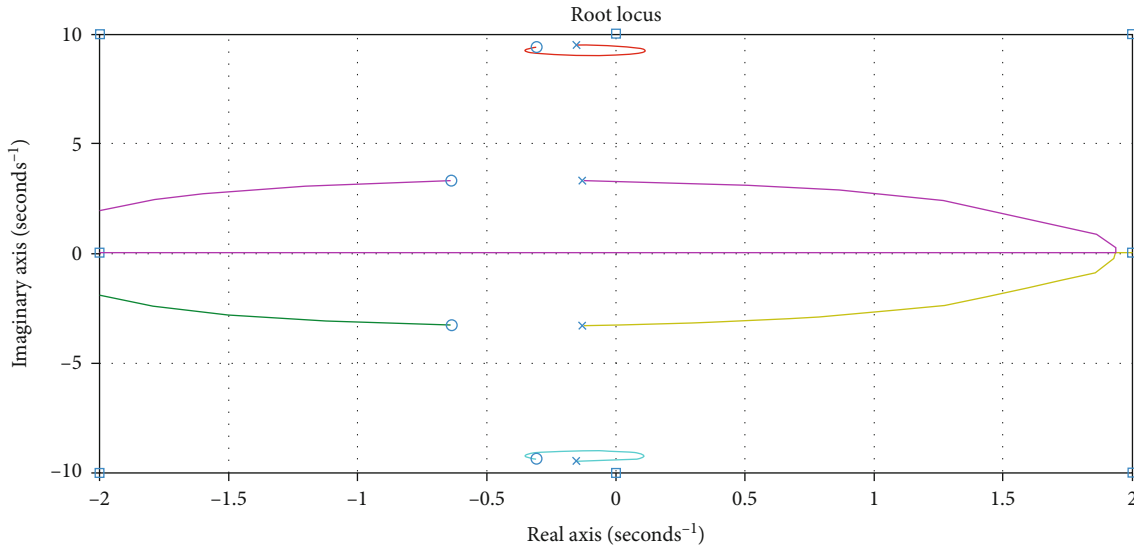


FIGURE 8: Zoomed view of the dominant poles of the transfer function in the Root Locus.

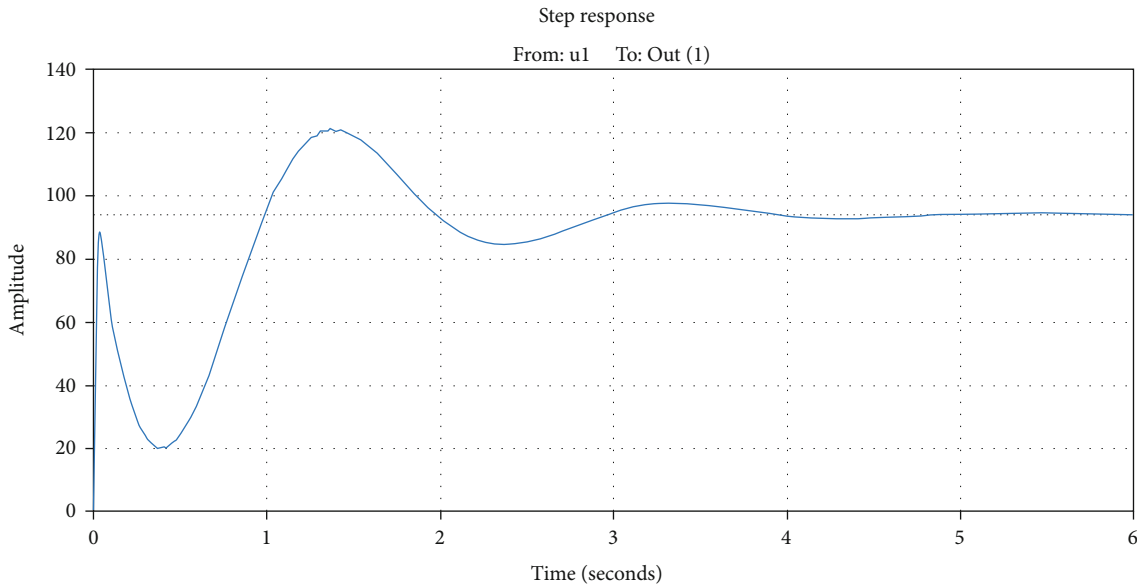


FIGURE 9: Step response of sys1.

- (iv) *Combination 4.* Q2 = active and Q3 = active. This mode of operation is not used, and it is prohibited as it may lead to a short circuit of the voltage across capacitor C2. In this research, the battery management circuit is operational either in the buck mode or in the boost mode. In the buck mode of operation, the intermediate link voltage across C2 is used to charge the LV battery. In the boost mode, the LV battery is the source, the main input source V_{in} is not available and is absent

2.3. Stability Analysis of the Proposed System Using Root Locus and Bode Plot. The stability of the two-stage super lift

converter has been studied using the basic cybernetic analytical tools like the Bode plot and the Root Locus plot. The transfer functions of the converter for different operational modes have been drawn between the output voltage V_{out} and the duty cycles of the switches active in each mode of operation. The transfer functions have been estimated using MATLAB commands. In this regard, two experiments have been conducted. In the first experiment, the buck boost converter section has been completely disconnected. A step change in duty cycle from 0.3 to 0.6, occurring at time instant 1 second, for the power electronic switch Q1 has been applied. The model was run for the period from 0 second to 2 seconds. The system has been simulated with an input voltage of 18 V with a load resistor of 48 Ohms and

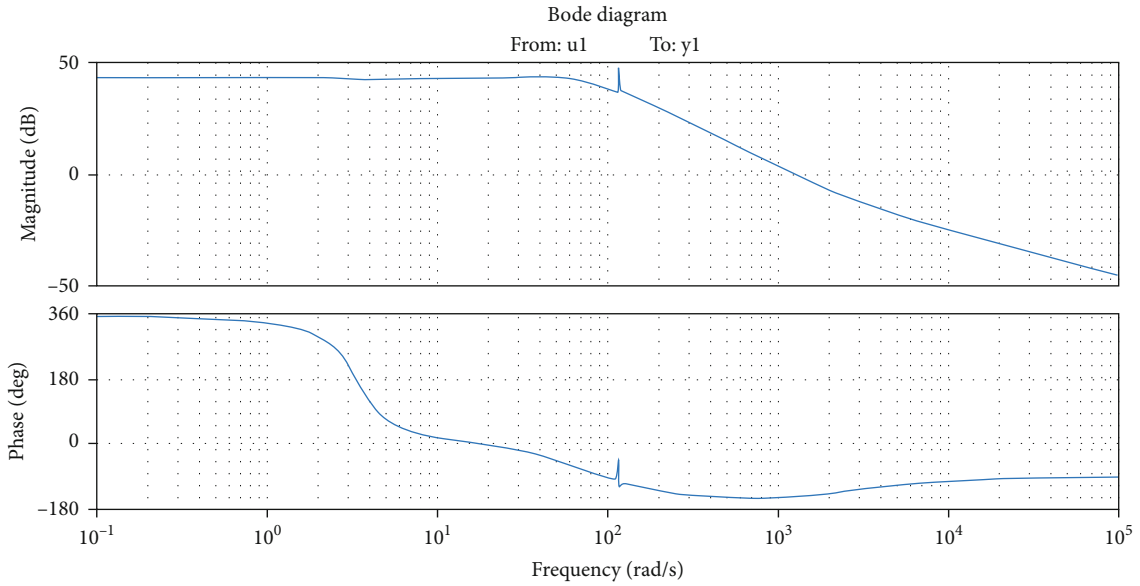


FIGURE 10: Bode plot of sys1.

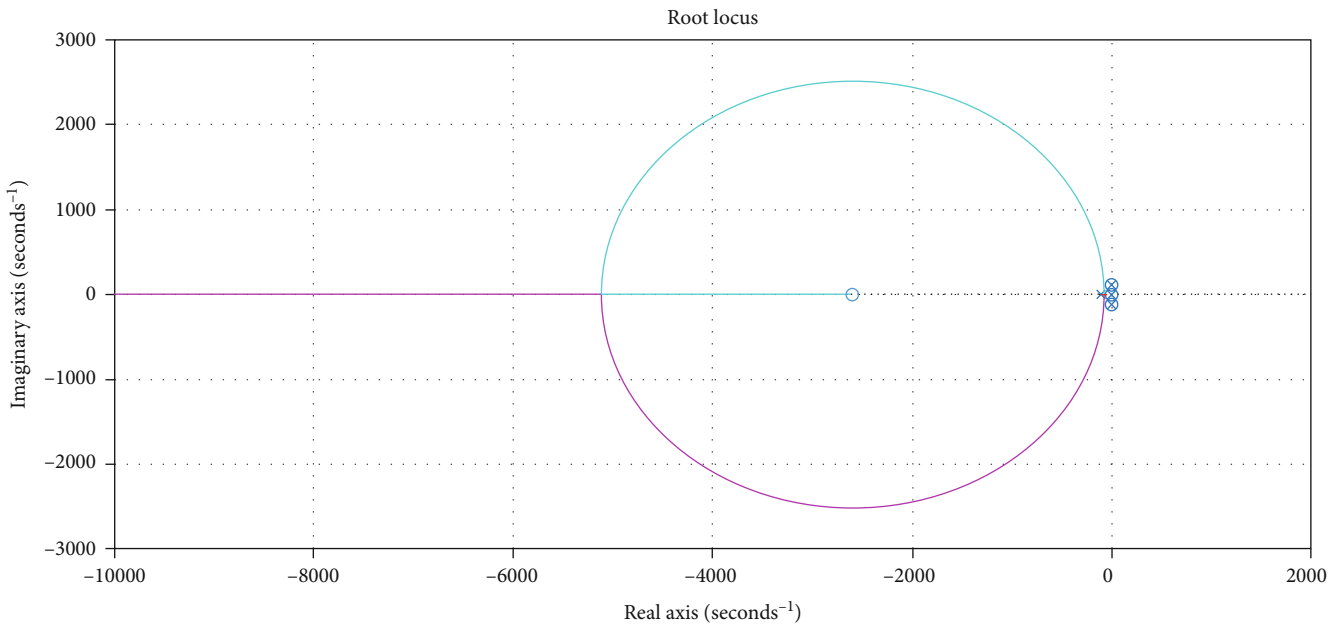


FIGURE 11: Root Locus of sys1.

a switching frequency of 5 kHz. The variables ‘Vout’ and ‘duty’ were collected in the MATLAB work space and the following commands were invoked from the MATLAB command line and the transfer function has been obtained.

```
>mysys = iddata (vout,duty,0.0001).
>sys = tfest (mysys,6).
```

$$\text{sys} = \frac{-3.137 \cdot 10^6 s^5 - 4.624 \cdot 10^8 s^4 - 1.176 \cdot 10^9 s^3 - 4.612 \cdot 10^{10} s^2 - 5.749 \cdot 10^{10} s - 4.529 \cdot 10^{11}}{s^6 + 7.665 \cdot 10^4 s^5 + 2.132 \cdot 10^6 s^4 + 8.899 \cdot 10^6 s^3 + 2.128 \cdot 10^8 s^2 + 1.304 \cdot 10^9 s + 2.062 \cdot 10^9} \quad (7)$$

TABLE 1: The specifications of the solar PV source.

Parameters	Value
Nominal power rating	390 Watts
Open circuit voltage	22.07 V
Short circuit current	7.86 A * 3
Voltage at Pmax	17.38 V
Current at Pmax	7.43 A * 3
Vpmax/Voc	0.7875
Test condition	1000 Watts/m ² ; 25°C

The transfer function is denoted by the variable *sys*. The commands `step (sys)`, `bode (sys)`, and `rlocus (sys)` give the step response, the Bode plot, and the Root Locus, respectively. The plot of the step response for duty cycle of 0.6 is shown in Figure 5.

(i) `step (0.6*sys)`

With the obtained transfer function ‘*sys*,’ the Root Locus plot and the Bode plot were also drawn. The Root Locus reveals that there are six poles and five zeros. All these poles are on the negative half of the complex plane. There are only four dominant poles, and two poles are far away from the *Y* axis and are less dominant. The four poles near the *Y* axis form two complex conjugate formation, and there are two corresponding spikes shown in the Bode plot as shown in Figure 6. Since all the poles are on the left half plane of the complex plane, the two-stage super lift Luo converter in which the output voltage is governed by the duty cycle is sta-

ble. The Root Locus and the zoomed view of the poles of the root locus are, respectively, shown in Figures 7 and 8.

In the following pages, the transfer function for the second mode of operation is derived. In this mode of operation, the main source is not available. The relatively low-voltage source drives the HV channel of the system. The transfer function relating the duty cycle of the boost converter applied at switch Q3, for a fixed duty cycle of the super lift Luo converter applied at Q1, and a fixed low-voltage source while the main input V_{in} is absent is derived. The transfer function between the output voltage and the duty cycle used for the boost switch Q3 while the buck switch Q2 is off is derived. The main input source V_{in} is not available, and the only source is the battery. The battery voltage is 12 V.

In this experiment, the boost converter stage with switch Q3, powered by a battery, drives the second part of the lift converter stage. Since it is assumed that no external source is available the lift stage in the front end is completely disconnected, the system has been simulated with a battery voltage of 12 V, a load resistor of 48 Ohms, and a switching frequency of 5 kHz. A step change in duty cycle from 0.3 to 0.6 has been applied for Q3, Q2 is turned off, and Q1 is maintained at a fixed duty cycle of 0.5. The step change in duty cycle for Q3 occurs at time instant 1 second from $D = 0.3$ to $D = 0.6$. The model was run for the period from 0 second to 2 second. The output voltage denoted as ‘*vout1*’ and the duty cycle for Q3 denoted as ‘*duty1*’ were collected in the work space and the following commands were invoked from the MATLAB command line and the transfer function has been obtained.

```
>mysys1 = iddata (vout1,duty1,0.0001).
>sys1 = tfest (mysys1,7)
```

$$sys1 = \frac{556.7.S^6 + 1.471 * 10^6 S^5 - 7.328 * 10^7 S^4 + 1.977 * 10^{10} S^3 + 8.649 * 10^{11} S^2 - 1.532 * 10^{12} S + 1.048 * 10^{13}}{S^7 + 208.8 S^6 + 2.89 * 10^4 S^5 + 3.302 * 10^6 S^4 + 2.081 * 10^8 S^3 + 6.43 * 10^9 S^2 + 1.461 * 10^{10} S + 6.6828 * 10^{10}} \quad (8)$$

Since *sys1* is the name of the transfer function the commands `step (sys1)`, `bode (sys1)` and `rlocus (sys1)` give the step response of the Bode plot and the Root Locus, respectively. The plot of the step response of the obtained transfer function *sys1* for a duty cycle of 0.6 gives an output as shown in Figure 9. The bode plot and the root locus are shown in Figures 10 and 11. The plot of the bode diagram and the root locus reveals that the system *sys1* is stable.

(ii) `Step (0.6*sys1)`

2.4. Design of Critical Components. The critical components in the front end lift stage are the inductor L1 and the capacitor C1. For the continuous conduction mode, the value of the inductor is found using the standard

$$L = \frac{(1 - D)^2 R}{2f}. \quad (9)$$

If D is 0.5 and R is the load resistance of 48 Ohms, with a switching frequency of 5 kHz, the value of L is

$$L_{CCM} = \frac{(1 - 0.5)^2 * 48}{2 * 5e3} = \frac{12}{10e3} = 12 \text{ mH}. \quad (10)$$

The value of the capacitance required for the filter is given by the general

$$C = \frac{(1 - D)}{8Lf^2}. \quad (11)$$

With a duty cycle of 0.5, the value of C can be found as

$$C = \frac{0.5}{8 * 12 * 10^{-3} * 25 * 10^6} = 2000 \text{ microfarad}. \quad (12)$$

All the inductors in the topology have been decided as

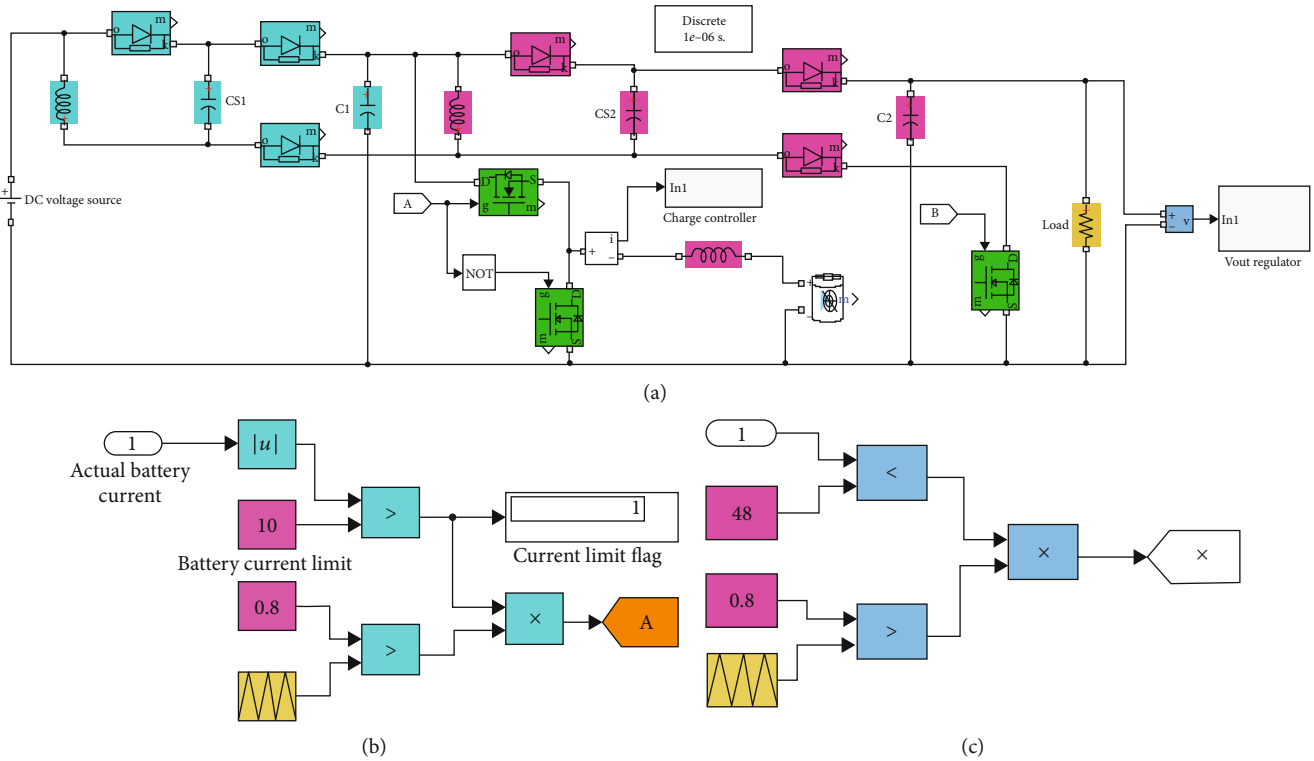


FIGURE 12: (a) Simulink implementation of the proposed system with a fixed DC. (b) Battery current regulation scheme. (c) Output voltage regulation scheme.

12mH, and the capacitors of value 2200 microfarad have been selected.

3. Maximum Power Point Tracking

The specifications of the solar photovoltaic source for the standard test condition of 1000 Watts/m^2 of solar irradiance and 25° centigrade areas are shown in Table 1. There exists a certain point corresponding to the V_{pmax} and I_{pmax} which, when maintained, guarantees maximum power harvest for the given climatic condition. Whenever the climatic conditions change, the terminal voltage of the SPV module and the PV current have to be changed to the new optimal position. The ratio between V_{pmax} and the V_{oc} corresponding to a particular irradiance and temperature is a constant K of the panel, and this ratio should be maintained for all solar irradiance and temperature. The sliding mode controller- (SMC-) based maximum power point tracking (MPPT) uses this principle.

The maximum power harvest can be obtained only when the terminal voltage of the SPV module is maintained at 17.38 V at this environmental condition. For changes in the solar irradiance, the optimal terminal voltage to be maintained is different and is governed by the factor K and the open circuit voltage of the SPV module at that solar irradiance. The steps involved in the sliding mode controller- (SMC-) based MPPT are to first keep the power control

switch in the off state and measure the V_{oc} . Then, find $V_{pmax} = V_{oc} * K$. Then, apply the switching pulses. Then, measure again V_{pv} . If V_{pv} is found to be less than $K * V_{oc}$ then turn off switching pulses, else keep on the switching pulses while monitoring V_{pv} . The results of the simulation with two different solar irradiances have been recorded and presented under the simulations section.

3.1. Sliding Mode Controller for Regulation of the Output Voltage. The sliding mode controller is a typical nonlinear controller suitable for the regulation of a parameter expected out of a system or plant that is fundamentally of a nonlinear nature. A power electronic converter typically uses a number of switches and diodes, and they are usually nonlinear systems. Since the power electronic switches can be discretely turned on and off, the two states of the switches form different topological structures which are independently linear. Thus, a power electronic converter is a variable structure system and the SMC could be a preferred one. Besides, the SMC does not require the exact model of the plant under control. The basic requirement of an SMC is that the controller should be able to bring the parameter under control from an initial value, say zero, to the neighborhood of the set point. After reaching the set point, the sliding action takes over to keep the controlled variable at the desired set value forever. The initial phase of bringing the controlled variable from an initial zero level to the vicinity of the set

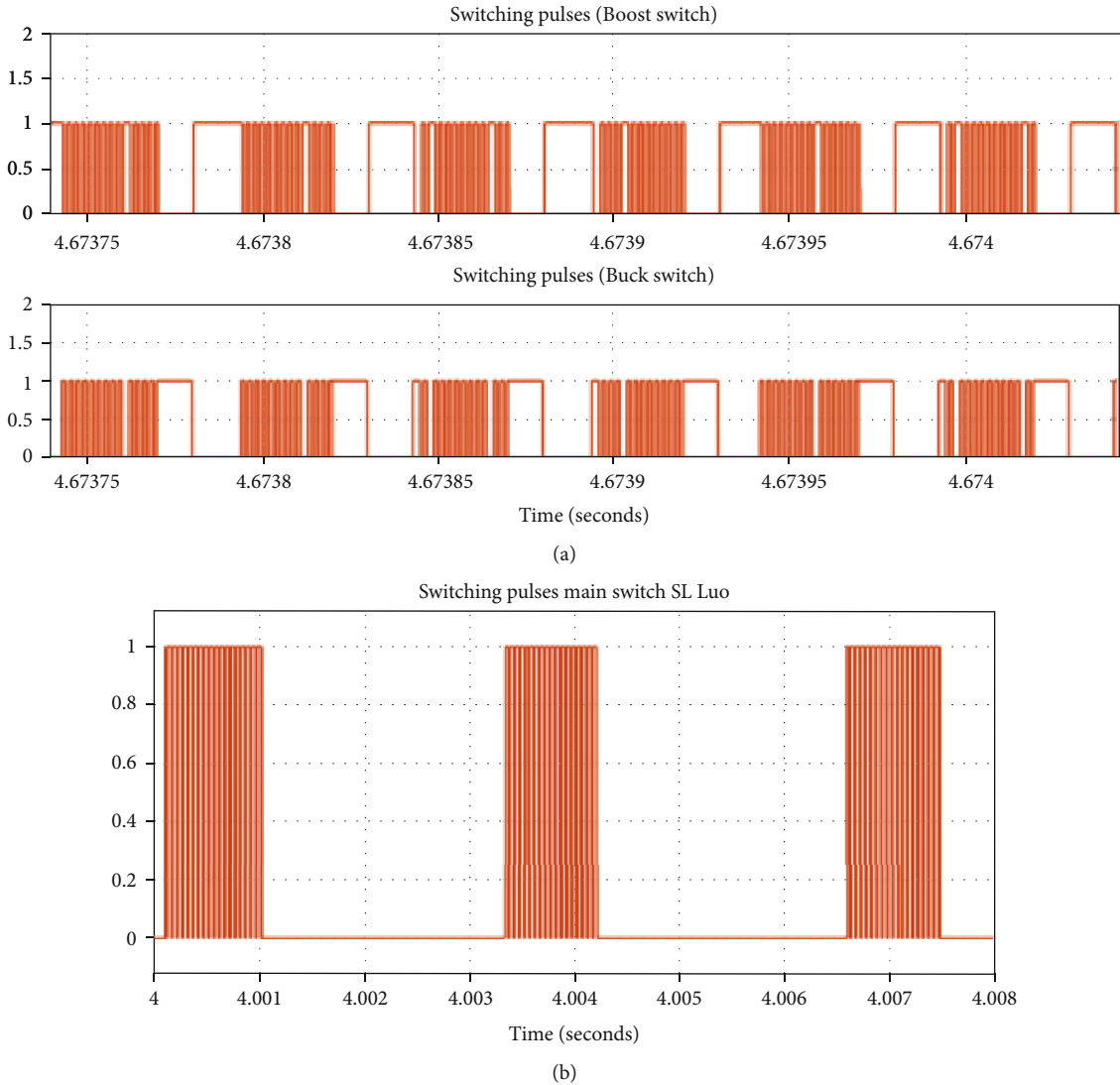


FIGURE 13: (a) Switching pulses for buck boost switches. (b) Switching pulses for relief Q1.

point is known as the reaching phase, and the second phase of control that keeps the controlled variable at the set point is the sliding phase.

The sliding mode controller, in its simplest form, is like a dead-beat controller where the manipulated parameter is fully turned on until the controlled parameter reaches the required level and is about to cross the set point and then turn off the manipulated parameter until the controlled parameter falls below and adheres to the set value. By an experiment, and as shown in Figure 3, it was found that the voltage gain becomes maximum when the duty cycle is 0.8. For all values of duty cycle below 0.8 and above 0.8, the voltage gain is falling while it is maximum only when the duty cycle is 0.8.

With reference to Figure 3, the relief Luo converter has been tested for duty cycles k continuously changed from 0 to 1. With a duty cycle $k=0$, the output voltage has remained to be equal to the input voltage $V_{in} = 12$. If $k = 0$,

the voltage gain becomes 1, and with $k = 1$, the theoretical voltage gain becomes infinity. However, because of the voltage drops occurring in the switches and diodes which are functions of the load current, as the duty cycle increases the current through the devices also increases, causing more on-state voltage drop and eventually reducing the voltage gain beyond the duty cycle $k = 0.8$. Therefore, the duty cycle that can give maximum voltage gain is found to be 0.8. A simple simulation to this effect has been carried out in the Simulink environment. A similar experiment was carried out in the experimental setup also, and it was observed in the experimental setup that the maximum voltage gain occurred at a duty cycle of $k = 0.65$. While using the SMC at the relief Luo converter, for regulating the output voltage, the fixed duty cycle of 0.8 is used. But the switching pulses with the 0.8 duty cycle are applied to the power control switch Q1 intermittently. The SMC decides the control flag that allows the switching pulses to Q1. The control flag is

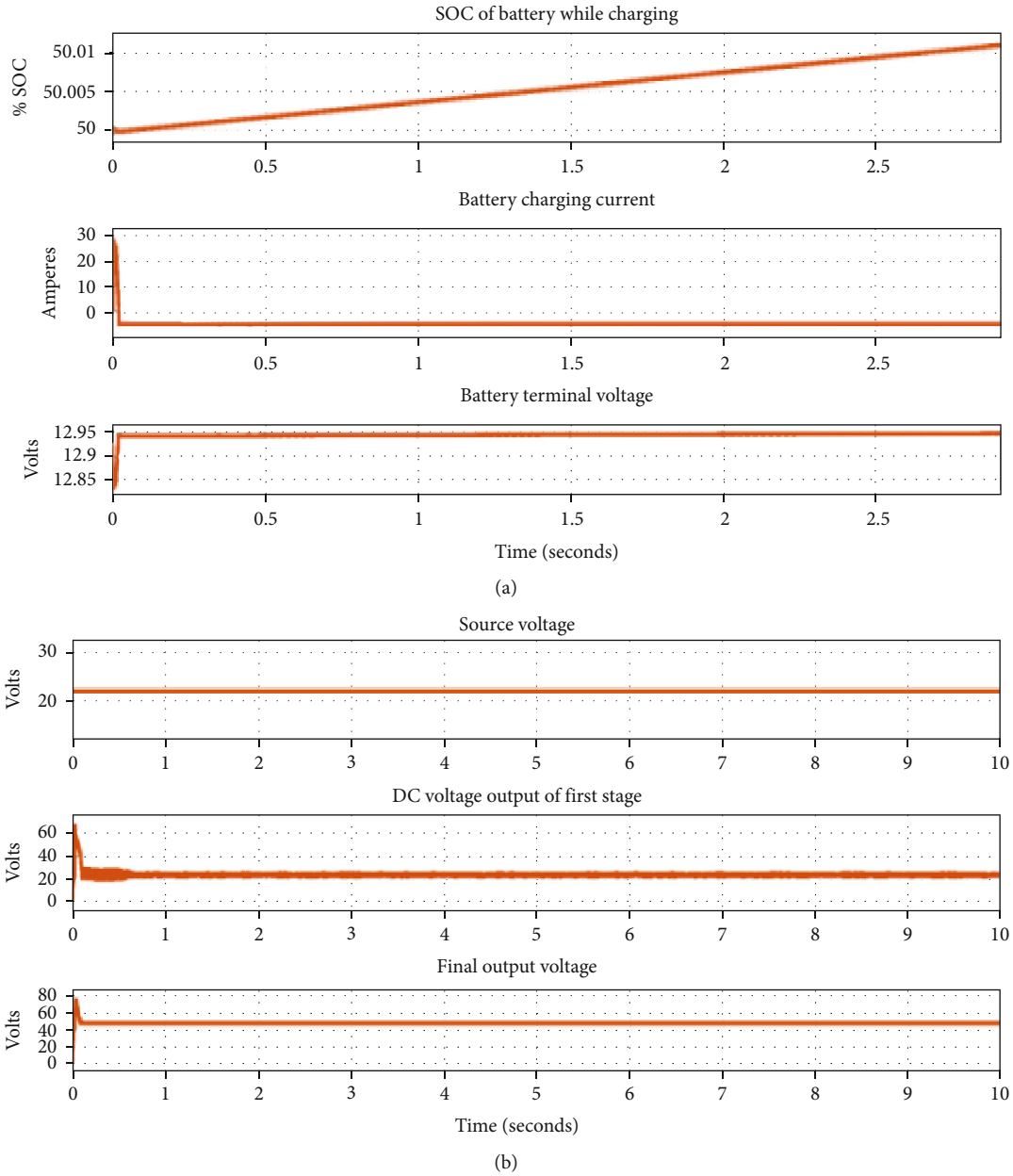


FIGURE 14: (a) SOC of battery I_{batt} and V_{batt} . (b) V_{pv} , V intermediate stage, and V_{out} .

logic high when the set value is more than the actual value, and the control flag is reset when the actual value just crosses above the set value. The SMC control law is therefore that the $\text{Flag} = 0$ while $(V_{\text{act}} > V_{\text{sp}})$ and $\text{Flag} = 1$ while $(V_{\text{act}} < V_{\text{sp}})$.

4. Realization of the Proposed System Using MATLAB Simulink

Figure 12(a) shows the implementation of the proposed system in MATLAB Simulink environment with a fixed DC source as the main input. As shown in Figure 12(b), the system has been provided with a battery charging control system with the charging current limited to 5 amperes. The

duty cycle has been kept at 0.8. The actual battery charging current is compared with the set value for the limit in the charging current. A control flag is thus created and that flag controls the application of the switching pulses to the buck boost converter. Figure 12(c) shows the implementation of the output voltage regulation subsystem that uses an SMC. The set value of 48 V is compared with the actual output voltage, and a control flag is generated. The switching pulses are generated by comparing a fixed duty cycle of 0.8 with a triangular carrier of 5 kHz. The switching pulses are allowed or not allowed to reach the gating circuit depending upon the control flag.

The proposed system with the solar PV source was implemented in MATLAB Simulink. The proposed system

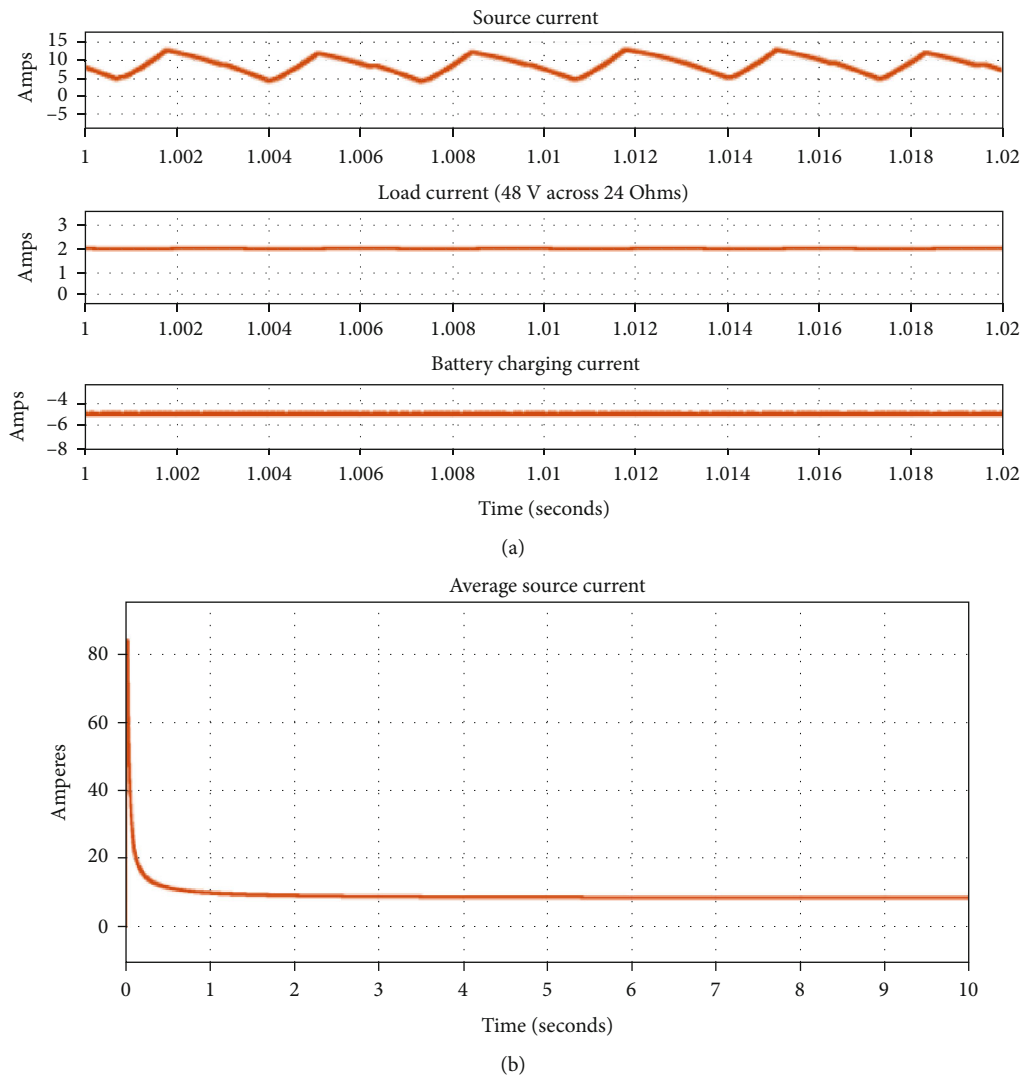


FIGURE 15: (a) Source, load, and battery currents. (b) The average source current.

also included an MPPT. The pilot panel is not used for supplying power to the load but is meant only to monitor the open circuit voltage of the solar photovoltaic panel. The generation of the control flag for MPPT was obtained using the SMC. Some of the interesting results and waveforms are presented herein.

Figure 13(a) shows the switching pulses for the switches Q2 and Q3, respectively, the buck and the boost switches forming the synchronous buck boost converter. Further, the switching pulses applied to the power control switch Q1 of the second stage of the relift converter are shown in Figure 13(b). When the battery is charged, the SOC of the battery gets increased as shown in Figure 14(a). The source voltage was kept at 24 V. The voltage at the output of the first stage is 36 V and this stage charges the battery, and the output voltage of the second stage is 48 V. The waveforms of the input voltage, the intermediate voltage, and the final output voltage across the load are shown in Figure 14(b).

With a load resistance of 24 V, the load current is 2 A. The battery charging current which is limited at 5 A and the source current which swings between 5 A and 13 A are shown in Figure 15(a). The average input current is 9 A as shown in Figure 15(b). The average power drawn from the source is $24\text{ V} \cdot 9\text{ A} = 216\text{ Watts}$. The power delivered to the load is $48\text{ V} \cdot 2\text{ A} = 96\text{ Watts}$. The power entering the battery is $12.94\text{ V} \cdot 5\text{ A} = 64.7\text{ Watts}$. The total power delivered to the load and the battery is 160.7 Watts while the input power is 216 Watts and the effective power conversion efficiency is 75%.

When the main source of power is not available, the battery becomes the source and it drives the 48 V load. The corresponding waveforms are shown in Figures 16(a) and 16(b). The fall of the SOC of the battery and battery discharged current and the terminal voltage across the battery are shown. The power drawn out from the battery in this mode is $12.9\text{ V} \cdot 4.9\text{ A} = 63.21\text{ Watts}$. With a load resistor of 48 Ohms, the load current was observed to be 1 A and the

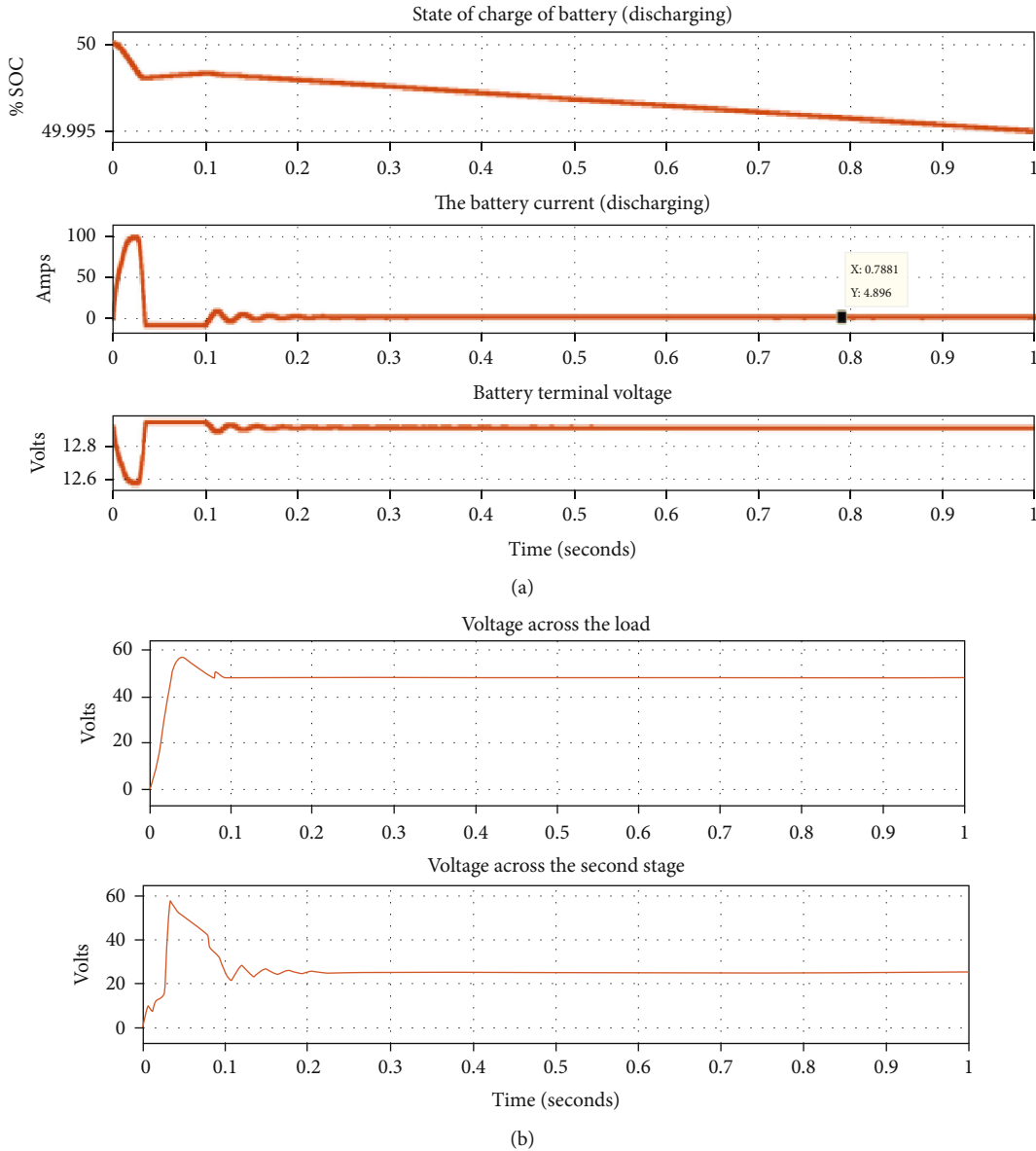


FIGURE 16: (a) Battery SOC, current, and terminal voltage. (b) Output of generic boost and final V_{out} .

power delivered to the load was found to be 48 Watts and the power conversion efficiency was 76%. The trajectories of the output voltage and the intermediate voltage while the battery is supplying and the intermediate voltage is that voltage that is given out by the synchronous buck boost converter while it acts in the boost mode powered by the battery.

When solar power is used as the main input source, the battery gets charged and the 48V load is also served. The power delivered by the solar PV source is a function of the solar irradiance. With a step fall in the solar irradiance from 1000 Watts/m² to 500 Watts/m² occurring at time instant of 1 second, the change in the battery charging current also gets changed as shown in Figures 17(a) and 17(b).

With two different solar irradiances of 1000 Watts/m² and 500 Watts/m², the power drawn from the solar PV

source is, respectively, 19 V*18 A = 342 Watts and 18 V*12 A = 216 Watts and the power transferred to the battery while charging has been 12.2 V*22 A = 268 Watts and 16.5 V*12.25 A = 202 Watts with a power conversion efficiency in both the cases, respectively, 78% and 93.3%. It has been observed that the maximum power conversion efficiency has been 93.3% while the solar insolation was 500 Watts/m².

From the simulations, it is observed that the peak to peak value of the ripple is a function of the load. With a regulated output voltage of 48 V across the load with a 48 Ohms resistance load, the output voltage was found to swing from 49.25 V to 47.75 V with a peak to peak ripple voltage of 1.5 V with a % ripple of 3.12%. When the load was reduced from 48 Ohms to 96 Ohms, the output voltage was observed to swing between 48 V and 49 V with a peak to peak ripple

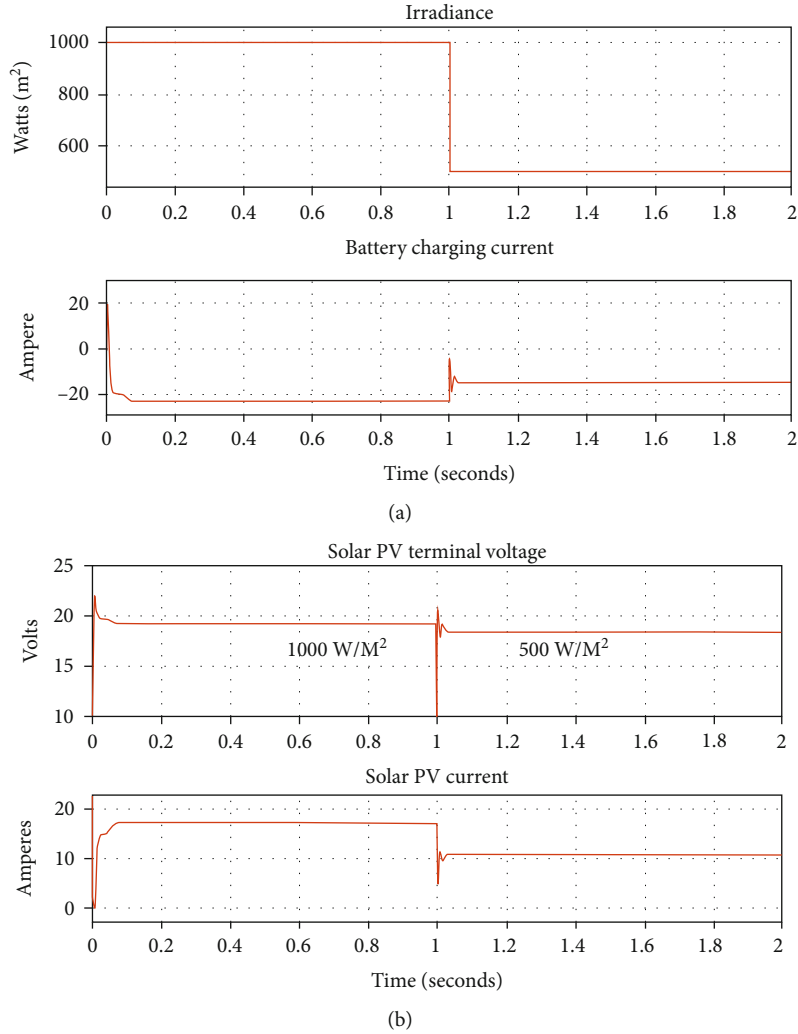


FIGURE 17: (a) Irradiance and charging current. (b) SPV voltage and current.

TABLE 2: Comparison of the time domain observations.

Load	Peak over shoot (volt)	Steady state error (volt)	Rise time (ms)	Integral square error
96 Watts	48.2	0.45	3	35.06
48 Watts	48.9	0.21	5	26.51
53 Watts	52	1.2	4	25.99
12 V	50	0.8	9	31.28
18 V	52	1.8	2.2	35.06
24 V	54	2.2	2	31.25

voltage of 1 V and the % ripple was 2%. With the 10% rise in load from 48 Watts to 53 Watts, the ripple voltage was found to rise to a peak to peak value of 1.7 V with a % ripple of 3.5%.

With the closed loop voltage regulation, for an input voltage of 18 V and the output maintained at 48 V, in action the time domain specifications like the peak overshoot, the steady state error, and the rise time were recorded for different loads. Similarly, with the closed loop voltage regulation, for changes in the input voltage between 12 V and 24 V with a fixed load of 48 Watts and the output maintained at 48 V, in action, the time domain specifications like the peak overshoot, the steady state error, and the rise time were recorded. Table 2 gives a comparison of the time domain observations for three different loads and three different input voltages.

5. Details of the Experimental Prototype

Figure 18 shows the photograph of the experimental setup. The specifications of the scaled down model are as shown in Tables 3 and 4. The prototype was developed with a solar PV source rated 125 Watts. The backup was provided by a battery rated with nominal terminal voltage of 12 V and 35 AH. Different experiments were carried out. The



FIGURE 18: Photograph of the prototype.

TABLE 3: Specifications of the SPV module used for the prototype.

Parameters	Value
Solar PV source	
Nominal power rating	125 Watts
Open circuit voltage per panel	22.07 V
Short circuit current	7.86 A
Voltage at Pmax	17.38 V
Current at Pmax	7.43 A
Volt at Pmax/volt Voc	$17.38/22.07 = 0.7875$
Test condition	1000 Watts/m ² ; 25°C

TABLE 4: The specifications of the SLLC, the battery, and the HV load.

Parameters	Value
Relift Luo converter	
Inductors L1-L3	12 mH
Capacitors C1-C5	2200 microfarad
Switches Q1-Q3	IRF 540
Diodes D1-D6	FR 607
Battery	12 V/35AH (lead acid)
HV 48 V load	48-24 E 48 W-96 W
Switching frequency	5 kHz

prototype was tested with the solar PV source while the battery was charged from the solar PV source and there was no load. Then, in the absence of the solar PV source, the battery was set to supply power to the load.

The important waveforms have been recorded, and some of them are presented herein. The switching pulses generated from the microcontroller PIC 16F877A were interfaced to the MOSFET through the optocoupler MCT 2E which is powered from an isolated power supply. With the solar power source available, the output voltage was regulated at 48 V. The sample of the output voltage and the set voltage were supplied to the microcontroller through the analog input channels A0 and A1 of the PIC microcontroller.

Figure 19 shows the waveform of the input DC voltage drawn from the solar PV source when the solar irradiance is fairly constant. The voltage level of the solar photovoltaic source is stepped up by the relift converter, and power is routed to the resistive load rated 96 Watts at 48 V with $R = 24$ Ohms. The relift converter can be considered a two-stage converter. The first stage steps up the input voltage to an intermediate voltage across an intermediate DC link capacitor. When the solar PV source is supplying power to the load while the battery was not connected, the complete power from the solar PV is delivered to the load with less losses. There are two inductors L1 and L2, respectively, in the first and the second stages of the relift Luo converter. It has been observed that the average voltage drop across an inductor is always zero.

When the load side voltage is 48 V, the load current is 2.4 A with a load resistance of 20 Ohms. The load current is modified by increasing the load resistance from 20 Ohms to 40 Ohms, and the results are recorded. The load was disturbed with a step rise and then a step fall, and the response was observed. In either case, the terminal voltage across the load was maintained at 48 V with a sharp disturbance occurring at the instants the load changed. The step fall in the load current has been obtained by changing the load resistance from 20 Ohms to 40 Ohms while the terminal voltage across the load was still regulated by the sliding mode controller at 48 V. When the load resistance was changed from 20 Ohms to 40 Ohms, the load current was reduced from 2.4 A to 1.2 A and this caused a disturbance in the terminal voltage and the sliding mode controller puts its back at 48 V. When the load resistance was changed from 40 Ohms to 20 Ohms, the load current was increased from 1.2 A to 2.4 A and this caused a disturbance in the terminal voltage and the sliding mode controller puts its back at 48 V.

When the load is fixed and the terminal voltage is being regulated at a desired voltage of 48 V, the disturbances occurring in the solar irradiance causes disturbances in the load side voltage and the load current. The disturbances caused to the load current because of fall and rise of solar irradiation have been recorded and a typical case is shown in Figure 20. When the output voltage was regulated at 48 V and the load resistance was 30 Ohms, the load current was observed to be 1.6 A. With a fall in the solar irradiance from 722 Watts/m² to 586 Watts/m², the step change in

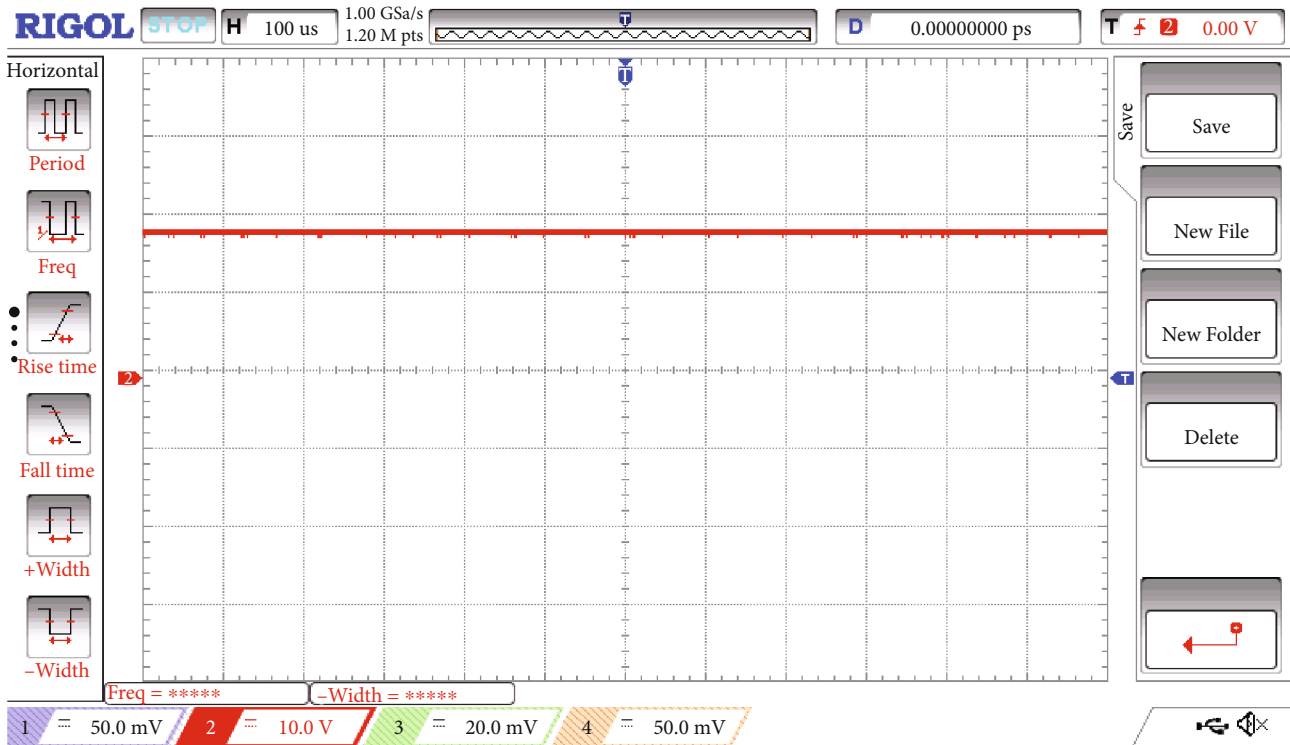


FIGURE 19: Solar PV terminal voltage.



FIGURE 20: Load current (step fall in irradiance).

the terminal voltage of the solar PV source has affected the regulation of the output voltage. In a similar manner with a step rise in the solar irradiance from 590 Watts/m² to 740 Watts/m², the output voltage was disturbed and restored

at the desired 48 V level, causing the load current to be regulated at 1.4 A with a load resistance of 35 Ohms. A switching frequency of 5 kHz was used at the main power control switch of the relift Luo converter for the regulation of the

TABLE 5: A comparison of the features of some of the dual-output DC to DC converters.

Type of Core	Switches	Diodes	Passive devices	V gain ($D = 0.5$)	Efficiency (%)
Ćuk-derived [21]	1	4	$L = 3, C = 4$	5	94
Boost-derived [22]	2	1	$L = 2, C = 2$	2	68
QBC-derived [23]	2	3	$L = 3, C = 4$	4	94
This article	3	6	$L = 3, C = 4$	9	93.3

output voltage. This caused the switching frequency triple across the output voltage. The ripple content of the output DC voltage amounting to 72 mV peak to peak has been observed. When the solar power source was absent, the battery was used to drive the load. The battery powered up the load with a terminal voltage of 48 V across a load resistor of 48 Ohms, delivering 48 Watts power output. The power supplied by the battery was discontinuous but had an average output current of 5.4 A, delivering a power of $12.2 \text{ V} \times 5.4 \text{ A} = 65.88 \text{ Watts}$. During this mode, the power conversion efficiency was found to be 74%.

With sufficient solar irradiance and while the state of charge of the battery was about 20%, the battery was charged and it exhibited an enormous voltage ripple across the battery. The voltage across the battery and the resulting charging current were recorded. The battery terminal voltage when the duty cycle was set manually to 50%. The terminal voltage of the weak battery is swinging with a large ripple above the DC level of 12 V. When the battery was discharged, while the solar PV source was not available, the inductor in the synchronous buck boost converter plays an important role, and the voltage drops across the inductor were observed. Although the voltage across the load is smooth with a ripple of just 75 mV peak to peak, the battery discharge current exhibits a strong swing. The inductor in the synchronous buck boost converter is the boost inductor at this stage. A comparison of the different multioutput DC to DC converters, particularly, the Ćuk-derived dual-output converter and the Boost-derived dual-output DC to DC converter as shown in Table 5.

6. Conclusion

A dual-output DC to DC converter with the relift Luo converter as the core converter has been presented in this article. The proposed system features two outputs with one output for driving a 48 V load and an auxiliary output to charge a battery. The main source of power is the solar photovoltaic source. It has been established that when the solar power is sufficiently available it can be used for charging the battery and power up the load. In the absence of the solar PV source, the battery has been used for driving the load. As compared to the existing boost-derived dual-output converter, the proposed scheme is proved to be more advantageous with increased voltage gain, which enables the system to be operational even with low solar irradiance or when the battery state of charge becomes very low. It has been shown that

the usage of the sliding mode controller for MPPT as well as for regulating the output voltage has been more effective.

Data Availability

The authors declare that they have no data copied from other sources.

Conflicts of Interest

The authors declare that they have no conflicts of interest.

References

- [1] Y. M. Chen, A. Q. Huang, and X. Yu, "A high step-up three-port DC-DC converter for stand-alone PV/battery power systems," *IEEE Transactions on Power Electronics*, vol. 28, no. 11, pp. 5049–5062, 2013.
- [2] B. R. Lin and C. W. Chu, "Hybrid DC-DC converter with high efficiency, wide ZVS range, and less output inductance," *International Journal of Circuit Theory and Applications*, vol. 44, no. 5, pp. 996–1011, 2016.
- [3] N. A. Dung, P. P. Hieu, Y. C. Hsieh, J. Y. Lin, Y. C. Liu, and H. J. Chiu, "A novel low-loss control strategy for bidirectional DC-DC converter," *International Journal of Circuit Theory and Applications*, vol. 45, no. 11, pp. 1801–1813, 2017.
- [4] A. Choudhury, P. Pillay, and S. S. Williamson, "Comparative analysis between two-level and three-level DC/AC electric vehicle traction inverters using a novel DC-link voltage balancing algorithm," *IEEE Journal of Emerging and Selected Topics in Power Electronics*, vol. 2, no. 3, pp. 529–540, 2014.
- [5] J. Malan and M. J. Kamper, "Performance of a hybrid electric vehicle using reluctance synchronous machine technology," *IEEE Transactions on Industry Applications*, vol. 37, no. 5, pp. 1319–1324, 2001.
- [6] R. Faraji and H. Farzanehfar, "Soft-switched non-isolated high step-up three-port DC-DC converter for hybrid energy systems," *IEEE Transactions on Power Electronics*, vol. 33, no. 12, pp. 10101–10111, 2018.
- [7] S. S. Dobakhshari, J. Milimonfared, M. Taheri, and H. Moradisizk, "A quasi-resonant current-fed converter with minimum switching losses," *IEEE Transactions on Power Electronics*, vol. 32, no. 1, pp. 353–362, 2017.
- [8] E. Babaei, Z. Saadatizadeh, and P. C. Heris, "A new topology for non-isolated multiport zero voltage switching dc-dc converter," *International Journal of Circuit Theory and Applications*, vol. 46, no. 6, pp. 1204–1227, 2018.
- [9] Z. Saadatizadeh, P. C. Heris, E. Babaei, and F. Sadikoglu, "Expandable interleaved high voltage gain boostDC-

- DCconverter with low switching stress,” *International Journal of Circuit Theory and Applications*, vol. 47, no. 5, pp. 782–804, 2019.
- [10] M. Mahmoudi, A. Ajami, and E. Babaei, “A non-isolated high step-up DC-DC converter with integrated 3 winding coupled inductor and reduced switch voltage stress,” *International Journal of Circuit Theory and Applications*, vol. 46, no. 10, pp. 1879–1898, 2018.
- [11] K. B. Park, G. W. Moon, and M. J. Youn, “Nonisolated high step-up boost converter integrated with SEPIC converter,” *IEEE Transactions on Power Electronics*, vol. 25, no. 9, pp. 2266–2275, 2010.
- [12] N. Kanagaraj, M. Ramasamy, H. Rezk, and T. Manesh, “Modified bi-directional DC-DC boost converter fed three-phase four-wire PV-DVR,” *Journal of Testing and Evaluation*, vol. 48, no. 4, pp. 1–29, 2018.
- [13] Y. P. Siwakoti, A. Mostaan, A. Abdelhakim et al., “High-voltage gain quasi-SEPIC DC-DC converter,” *IEEE Journal of Emerging and Selected Topics in Power Electronics*, vol. 7, no. 2, pp. 1243–1257, 2019.
- [14] K. Ravichandrudu, P. S. P. Kumar, and K. Seshu, *A high step-up three-port DC-DC converter for stand-alone PV/battery power systems*, Department of EEE, NRI Institute of Technology, International Journal of Science and Research (IJSR), Guntur, 2020.
- [15] N. Vázquez, C. M. Sanchez, C. Hernández, E. Vázquez, L. del Carmen García, and J. Arau, “A different three-port DC/DC converter for standalone PV system,” *International Journal of Photoenergy*, vol. 2014, Article ID 692934, 13 pages, 2014.
- [16] Y. Hu, W. Xiao, W. Cao, B. Ji, and D. J. Morrow, “Three-port DC-DC converter for stand-alone photovoltaic systems,” *IEEE Transactions on Power Electronics*, vol. 30, pp. 3068–3076, 2014.
- [17] N. R. Nair and P. Kanakasabapathy, “A three phase grid connected SPV system using synchronverter,” in *2018 8th IEEE India International Conference on Power Electronics (IICPE)*, Jaipur, India, 2018.
- [18] G. K. Taneja, G. Modi, B. Singh, and A. Verma, “GMCC based adaptive filter for SPV-RES to improve power quality in distribution grid,” in *2021 4th Biennial International Conference on Nascent Technologies in Engineering (ICNTE)*, NaviMumbai, India, 2021.
- [19] Y. Singh, I. Hussain, B. Singh, and S. Mishra, “Grid integration of single-phase single-stage SPV system using an active noise isolation based control algorithm,” in *2016 IEEE International Conference on Power Electronics, Drives and Energy Systems (PEDES)*, Trivandrum, India, 2016.
- [20] V. S. Mahadik and P. K. Katti, “Performance enhancement of SPV based water pumping with multifunction converter,” in *2018 International Conference on Power Energy, Environment and Intelligent Control (PEEIC)*, Greater Noida, India, 2018.
- [21] V. F. Pires, A. Cordeiro, D. Foito, and J. F. Silva, “High step-up DC-DC converter for fuel cell vehicles based on merged quadratic boost-Ćuk,” *IEEE Transactions on Vehicular Technology*, vol. 68, no. 8, pp. 7521–7530, 2019.
- [22] O. Ray, A. P. Josyula, S. Mishra, and A. Joshi, “Integrated dual-output converter,” *IEEE Transactions on Industrial Electronics*, vol. 62, no. 1, pp. 371–382, 2015.
- [23] S.-W. Lee and H.-L. Do, “Quadratic boost DC-DC converter with high voltage gain and reduced voltage stresses,” *IEEE Transactions on Power Electronics*, vol. 34, no. 3, pp. 2397–2404, 2018.